International Journal of Solids and Structures 51 (2014) 4101–4112

Contents lists available at ScienceDirect

International Journal of Solids and Structures

journal homepage: www.elsevier.com/locate/ijsolstr

Material instability-induced extreme damping in composites: A computational study

Felix Fritzen [a], Dennis M. Kochmann [b,*]

[a] Young Investigator Group Computer Aided Material Modeling, Chair for Continuum Mechanics, Institute of Engineering Mechanics, Karlsruhe Institute of Technology (KIT), Kaiserstr. 10, D-76131 Karlsruhe, Germany

[b] Graduate Aerospace Laboratories, California Institute of Technology, Pasadena, CA 91125, USA

ARTICLE INFO

Article history:
Received 4 April 2014
Received in revised form 13 July 2014
Available online 14 August 2014

Keywords:
Viscoelasticity
Material instability
Homogenization
Composite
Finite elements

ABSTRACT

We investigate the effective viscoelastic performance of particle-reinforced composite materials whose particulate phase undergoes a material instability resulting in temporarily non-positive-definite elastic moduli. Recent experiments have shown that phase transitions in geometrically-constrained composite phases (such as in particles embedded in a stiff matrix) can lead to stable non-positive-definite elastic moduli, and they hinted at strong damping increases that can be achieved from such metastable composite phases. All previous theoretical efforts to explain such phenomena have used simplistic one-dimensional models or they were based on composite bounds and specific two-phase solids. Here, we study particle–matrix composites with periodic randomized particle dispersion. A finite element discretization is used in combination with a sophisticated nonlinear solver in order to perform the numerous calculations in a feasible amount of computing time. Our computational analysis shows that stable non-positive-definite inclusion moduli can indeed lead to extreme damping increases (i.e. greatly exceeding the intrinsic damping of each composite phase) and that such extreme damping arises from a shift in microstructural mechanisms.

1. Introduction

Composite materials are a popular means to achieve beneficial combinations of material properties that are naturally exclusive. A prime example is the combination of high stiffness and high damping which, due to contrary microstructural mechanisms, is a rare find albeit of utmost importance to a myriad of technological and scientific applications. A common solution is to integrate a stiff phase with a lossy one, whose base material properties, their volume fractions, geometric arrangement, and bonding define the overall composite properties. The effective material performance can be estimated via composite bounds (see e.g. Milton (2002) for an overview of bounds on the viscoelastic properties of composite) as well as through computational studies that aim at extracting the effective macroscale response from averaging over a representative microscale configuration. The quality of such estimates depends primarily on the level of microstructural details represented by the model.

The classical composite bounds of, e.g. Voigt (1889) and Reuss (1929) as well as those of Hashin and Shtrikman (1963) for isotropic solids suggest that the combination of two or more phases into a composite can only result in a compromise of the individual properties of the constituent base materials. In other words, the effective stiffness and damping of a composite cannot surpass the stiffness or damping of any of the composite constituents, respectively. Various authors have reported techniques to identify geometric arrangements of composite constituents to result in optimal effective performance – within the aforementioned bounds. Rather recently, it was shown that non-positive-definite elastic phases (often referred to as *negative-stiffness* phases) in composites can lead to extreme effective behavior, where *extreme* denotes properties that significantly surpass those of all constituent materials (Lakes and Drugan, 2002; Wojnar and Kochmann, 2014). Non-positive-definite (visco)elastic moduli are unstable in solids with mixed or pure-traction boundary conditions (e.g. in free-standing solids) (Kirchhoff, 1859) but can be stabilized if sufficiently constrained, e.g. as particles embedded in a matrix or coating that is sufficiently stiff and thick (see e.g. Drugan, 2007; Kochmann and Drugan, 2009, 2012; Kochmann, 2012). A loss of elastic positive-definiteness occurs, among others, during second-order phase transitions (Jaglinski and Lakes, 2007) when the

* Corresponding author. Tel.: +1 626 395 8113; fax: +1 626 395 2900.
E-mail addresses: felix.fritzen@kit.edu (F. Fritzen), kochmann@caltech.edu (D.M. Kochmann).

http://dx.doi.org/10.1016/j.ijsolstr.2014.07.028
0020-7683/

single-well free energy landscape transforms into a multi-well energy (Landau, 1937) while the solid is kept from transforming due to the geometric constraints (i.e. the local curvature of the energy landscape becomes negative, implying non- positive-definite incremental elastic moduli). For example, Dong et al. (2010a) measured the isotropic linear viscoelastic moduli of pure unconstrained barium titanate ($BaTiO_3$), a ferroelectric ceramic showing a martensitic transformation near 120 °C, undergoing time-harmonic bending using Broadband Viscoelastic Spectroscopy (BVS). Their results, shown in Fig. 1, illustrate the pronounced softening of the dynamic viscoelastic moduli and, in particular, a strong softening of the dynamic bulk modulus close to 0 GPa near the transition temperature at low mechanical frequencies (here, at 0.1 Hz). After metal-coating the $BaTiO_3$ specimen, the softening of Young's modulus is even more pronounced (see also Dong et al., 2010b). Of course, these results do not show any stable negative bulk or shear moduli because these would be unstable and thus thermodynamically inadmissible. However, experiments on $BaTiO_3$ particles embedded in a metal matrix have demonstrated extreme increases in the dynamic stiffness and damping near the transition temperature of the particles (Jaglinski et al., 2007). Considering the classical bounds on composite properties, such strong increases can best be explained by a temporarily non-positive-definite inclusions phase (see e.g. Jaglinski et al., 2007). Similar phenomena have been reported e.g. for metal-matrix composites containing VO_2 inclusions (Lakes et al., 2001).

Despite the aforementioned experimental evidence, a fundamental understanding of the underlying microstructural mechanisms that lead to extremely high damping is incomplete. Previous studies fall into one of three categories. (i) Investigations based on composite bounds have relied upon the correspondence principle (see e.g. Lakes, 2001a,b; Kochmann, 2014) which is based on strong restrictive assumptions and may loose validity in complex multi-phase composites (Milton, 2002). (ii) Theoretical and computational studies of one- and two-dimensional spring-dashpot assemblies (Wang and Lakes, 2004a,b; Wang et al., 2006) have also predicted high damping due to negative-stiffness elements but do not readily admit extension to complex three-dimensional composite materials. (iii) Investigations of specific two-phase bodies (such as coated spheres and cylinders) have confirmed strong damping increases in the presence of negative stiffness (Kochmann, 2014); yet, they do not allow for qualitative or quantitative predictions for general composite materials with periodic or random microstructure.

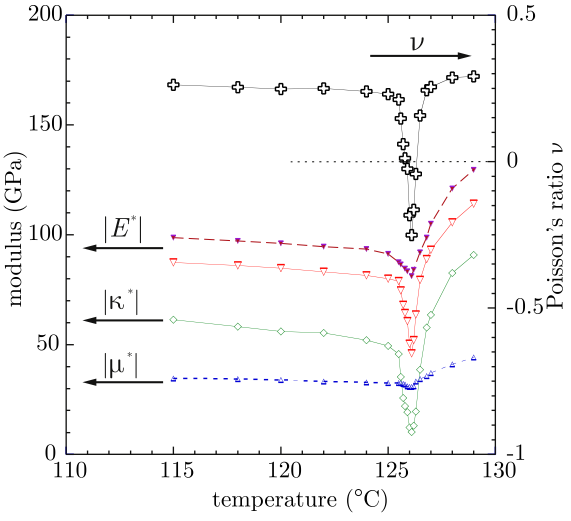

Fig. 1. Mechanical softening of the dynamic viscoelastic moduli of pure and coated $BaTiO_3$ near the phase transformation at 0.1 Hz, adopted from Dong et al. (2010a).

In order to extend the previous research towards a better understanding of the aforementioned damping phenomena, we investigate the effective linear viscoelastic moduli of particle–matrix composites by a computational two-scale approach. The ceramic inclusion phase is modeled as a linear viscoelastic solid embedded in a linear viscoelastic matrix. The viscoelasticity within both phases is described by generalized Maxwell models. We assume a random dispersion of particles and extract the effective material response to time-harmonic excitation by methods of homogenization. Frequencies are kept sufficiently low to avoid the influence of resonance and to allow us to neglect inertial effects. We choose the specific example material system studied experimentally by Jaglinski et al. (2007): ceramic inclusions in a matrix of pure tin. Since the intricate mechanisms of the underlying phase transitions go beyond the scope of this contribution, we assign non-positive-definite linear elastic moduli to the inclusion phase and explore the resulting macroscopic response for the full range of stable moduli, where stable refers to the stability of the effective composite material. Note that for isotropic solids (characterized by their shear and bulk moduli) we only consider negative values of the bulk modulus. A negative shear modulus necessarily implies local instability due to a loss of strong ellipticity (Hadamard, 1903).

The detailed geometric description of the representative unit cell as well as the necessity to compute the mechanical response over several load cycles at low mechanical frequencies result in enormous computational expenses. In order to speed up the solution of the high dimensional linear systems found during the finite element study, a modified Krylov method based on a preconditioned conjugate gradient (CG) method is used.

This paper is structured as follows. In Section 2 we describe the variational constitutive models as well as the computational two-scale approach to determine the effective mechanical properties of the composite material. In Section 3, we summarize results for the effective dynamic response and discuss the underlying physical mechanisms, before Section 4 concludes our analysis.

2. Multiscale model of linear viscoelastic composites

2.1. Notation and mechanical framework

In the following, we use an index-free notation for conciseness. Lower-case symbols denote scalars (e.g. $c,\ \psi,\ \phi$), lower-case boldface characters represent vectors (e.g. $\boldsymbol{x}$, $\boldsymbol{u}$), and upper-case Latin letters (e.g. $\boldsymbol{A}$, $\boldsymbol{I}$) and lowercase bold-face Greek letters (e.g. $\boldsymbol{\sigma}$, $\boldsymbol{\varepsilon}$) are used to identify second-order tensors. Fourth-order tensors are indicated by double-stroke symbols (e.g. $\mathbb{C}, \mathbb{P}$).

The focus of our investigation is on the linear viscoelastic properties of composites in response to time-harmonic vibrational loads. We assume that the excitation is sufficiently small to prevent the activation of inelastic material processes such as plasticity or damage, although these may play an important role in understanding the long-term stability of the composites investigated here. However, the consideration of these material nonlinearities is beyond the scope of our analysis. We further assume that a linear viscoelastic description is appropriate. Given the transient displacement field $\boldsymbol{u}(\boldsymbol{x},t)$ at a point $\boldsymbol{x}\in\Omega\subset\mathbb{R}^3$ within a body Ω at time $t\in[0,T]$, the infinitesimal strain tensor

$$\boldsymbol{\varepsilon}(\boldsymbol{x},t)=\operatorname{sym}\left[\operatorname{grad}\left(\boldsymbol{u}(\boldsymbol{x},t)\right)\right] \tag{1}$$

describes the local kinematics of the solid. A constitutive relation is assumed to relate the strain history up to time t to the symmetric Cauchy stress tensor $\boldsymbol{\sigma}(\boldsymbol{x},t)$. With mass density $\varrho(\boldsymbol{x},t)$ and an

external body force field $\boldsymbol{b}(\boldsymbol{x},t)$, the motion of the solid is governed by the balance of linear and angular momentum, and mechanical equilibrium is attained if

$$\left.\begin{aligned} \operatorname{div}(\boldsymbol{\sigma}(\boldsymbol{x},t)) + \boldsymbol{b}(\boldsymbol{x},t) &= \varrho(\boldsymbol{x},t)\,\ddot{\boldsymbol{u}}(\boldsymbol{x},t) \\ \boldsymbol{\sigma}(\boldsymbol{x},t) &= (\boldsymbol{\sigma}(\boldsymbol{x},t))^{\mathsf{T}} \end{aligned}\right\}. \tag{2}$$

Here and in the following, dots denote differentiation with respect to time. In the following inertial effects and body forces are neglected. This is justified since the mechanical loading will be sufficiently slow to avoid resonant effects, and typical experimental specimens are on the order of millimeters so that gravitational effects can be neglected. The system of equations is complemented by initial conditions for the displacement field $\boldsymbol{u}(\boldsymbol{x},t)$ and the velocity field $\dot{\boldsymbol{u}}(\boldsymbol{x},t)$. Further, appropriate boundary conditions of Dirichlet type ($\boldsymbol{u}(\boldsymbol{x},t)$ prescribed on Γ_u) and of Neumann type (traction vector $\boldsymbol{t}(\boldsymbol{x},t) = \boldsymbol{\sigma}(\boldsymbol{x},t)\boldsymbol{n}(\boldsymbol{x})$ prescribed on Γ_t with outward unit normal $\boldsymbol{n}(\boldsymbol{x})$) are assumed.

2.2. Variational constitutive model

In order to close the system of equations, the constitutive equations relating the strain history to the current Cauchy stress are required. A potential-based model in the spirit of standard dissipative solids (e.g. Germain, 1973; Halphen and Nguyen, 1975; Perić, 1993; Ortiz and Stainier, 1999) with internal state variables $\mathcal{I}$, the Helmholtz free energy density $\psi(\boldsymbol{\varepsilon},\mathcal{I})$ and the dissipation potential $\phi(\dot{\boldsymbol{\varepsilon}},\dot{\mathcal{I}})$ is assumed in the following. The stress tensor $\boldsymbol{\sigma}$ decomposes into an equilibrium contribution $\boldsymbol{\sigma}_0$ (which derives from the Helmholtz free energy density) and a viscous contribution $\boldsymbol{\sigma}_v$:

$$\boldsymbol{\sigma}(\boldsymbol{\varepsilon},\dot{\boldsymbol{\varepsilon}},\mathcal{I},\dot{\mathcal{I}}) = \boldsymbol{\sigma}_0(\boldsymbol{\varepsilon},\mathcal{I}) + \boldsymbol{\sigma}_v(\dot{\boldsymbol{\varepsilon}},\dot{\mathcal{I}}), \tag{3}$$

$$\boldsymbol{\sigma}_0(\boldsymbol{\varepsilon},\mathcal{I}) = \frac{\partial\psi(\boldsymbol{\varepsilon},\mathcal{I})}{\partial\boldsymbol{\varepsilon}}. \tag{4}$$

The generalized vector of thermodynamic driving forces $\mathcal{F}$ is obtained via

$$\mathcal{F} = -\frac{\partial\psi(\boldsymbol{\varepsilon},\mathcal{I})}{\partial\mathcal{I}}. \tag{5}$$

The dissipation potential provides the algebraic constraints

$$\boldsymbol{\sigma}_v(\dot{\boldsymbol{\varepsilon}},\dot{\mathcal{I}}) = \frac{\partial\phi(\dot{\boldsymbol{\varepsilon}},\dot{\mathcal{I}})}{\partial\dot{\boldsymbol{\varepsilon}}}, \quad \mathcal{F} = \frac{\partial\phi(\dot{\boldsymbol{\varepsilon}},\dot{\mathcal{I}})}{\partial\dot{\mathcal{I}}}. \tag{6}$$

Eqs. (5) and (6) lead to the Biot-type evolution law for the internal variables, viz.

$$\frac{\partial\psi(\boldsymbol{\varepsilon},\mathcal{I})}{\partial\mathcal{I}} + \frac{\partial\phi(\dot{\boldsymbol{\varepsilon}},\dot{\mathcal{I}})}{\partial\dot{\mathcal{I}}} = 0, \tag{7}$$

where differentiable potentials are assumed. Examples for the internal variables $\mathcal{I}$ include a viscous or plastic strain tensor, or hardening variables. The viscous non-equilibrium stress $\boldsymbol{\sigma}_v$ commonly stems from purely viscous effects. The simplest scenario is a linear relation between the total strain rate $\dot{\boldsymbol{\varepsilon}}$ and the viscous stress $\boldsymbol{\sigma}_v$ as found, e.g. in the popular Kelvin–Voigt model of viscoelasticity or in Newtonian fluids.

2.3. Microscale: linear viscoelastic material model

In this study we focus on isotropic, linear viscoelastic materials of generalized Maxwell type (Wiechert, 1893) (see e.g. Holzapfel and Simo, 1996; Fritzen and Böhlke, 2013 for recent extensions and applications). The experiments reported e.g. in (Lakes (2001a) and Jaglinski et al. (2007) demonstrated the observed extreme damping under quasistatic thermal loading while the time-harmonic mechanical loads vary at speeds that are orders of magnitude higher. This removes any transient effects and ensures a steady-state time-harmonic scenario. Furthermore, the experimentally observed phenomena due to the structural transition are not instantaneous but stable for certain periods of time. The loading frequency is significantly below any system-inherent resonance. For all those reasons, we choose to investigate the steady-state approach while neglecting inertial effects. Furthermore, the total transformation strains involved are less than 0.1% in magnitude (Kochmann, 2006). Experiments realized maximum surface strains on the order of 10^{-4}. Therefore, the observed phenomena can, to a first approximation, be represented by a linear theory.

The rheological model consists of n_M Maxwell elements with viscosities $\eta^{(m)}$ and shear stiffness values $G_v^{(m)}$ ($m = 1,\dots,n_M$). The ground elasticity is described by bulk modulus K_0 and shear modulus G_0, as shown in Fig. 2. Here and in the sequel, the two isotropic projectors in three dimensions are defined by

$$\mathbb{P}_1 = \frac{1}{3}\boldsymbol{I}\otimes\boldsymbol{I}, \quad \mathbb{P}_2 = \mathbb{I}^s - \mathbb{P}_1, \tag{8}$$

where $\boldsymbol{I}$ denotes the second-order identity tensor, and $\mathbb{I}^s$ is the identity on symmetric tensors. Note that all fourth-order tensors used throughout this manuscript have major and both minor symmetries. The viscosity is often expressed in terms of a relaxation time $\tau^{(m)}$ and the shear modulus $G_v^{(m)}$ via $\eta^{(m)} = G_v^{(m)}\tau^{(m)}$.

The viscous strains $\boldsymbol{\varepsilon}_v^{(m)}$ ($m = 1,\dots,n_M$) in the Maxwell elements form the internal variables $\mathcal{I} = \left\{\boldsymbol{\varepsilon}_v^{(1)},\dots,\boldsymbol{\varepsilon}_v^{(n_M)}\right\}$. We assume that only shear viscosity is observed, which results in the viscous strain tensors to be purely deviatoric, i.e. $\boldsymbol{\varepsilon}_v^{(m)} = \operatorname{dev}\left(\boldsymbol{\varepsilon}_v^{(m)}\right) = \mathbb{P}_2\,\boldsymbol{\varepsilon}_v^{(m)}$. The corresponding Helmholtz free energy density is introduced as

$$\psi(\boldsymbol{\varepsilon},\mathcal{I}) = \frac{1}{2}\boldsymbol{\varepsilon}\cdot\mathbb{C}_0\boldsymbol{\varepsilon} + \sum_{m=1}^{n_M} G_v^{(m)}\left\|\operatorname{dev}(\boldsymbol{\varepsilon}) - \boldsymbol{\varepsilon}_v^{(m)}\right\|^2 \tag{9}$$

with $\mathbb{C}_0 = 3K_0\mathbb{P}_1 + 2G_0\mathbb{P}_2$. It defines the stress $\boldsymbol{\sigma}$ and the driving forces $\boldsymbol{\sigma}_v^{(m)}$ conjugate to the viscous strains as

$$\boldsymbol{\sigma} = \frac{\partial\psi}{\partial\boldsymbol{\varepsilon}} = \mathbb{C}_0\boldsymbol{\varepsilon} + \sum_{m=1}^{n_M}\boldsymbol{\sigma}_v^{(m)}, \tag{10}$$

$$\boldsymbol{\sigma}_v^{(m)} = -\frac{\partial\psi}{\partial\boldsymbol{\varepsilon}_v^{(m)}} = 2G_v^{(m)}\left(\operatorname{dev}(\boldsymbol{\varepsilon}) - \boldsymbol{\varepsilon}_v^{(m)}\right). \tag{11}$$

Note that the special case of linear elasticity is obtained by choosing $G_v^{(m)} = 0$ for all $m = 1,\dots,n_M$. The dissipation function ϕ is taken to depend only on the rates of the internal variables according to

$$\phi\left(\dot{\boldsymbol{\varepsilon}}_v^{(1)},\dots,\dot{\boldsymbol{\varepsilon}}_v^{(n_M)}\right) = \sum_{m=1}^{n_M}\eta^{(m)}\left\|\dot{\boldsymbol{\varepsilon}}_v^{(m)}\right\|^2. \tag{12}$$

Finally, the Biot-type Eq. (7) relating (11) to (12), yields the evolution equations for the viscous strain tensors $\boldsymbol{\varepsilon}_v^{(m)}$, viz.

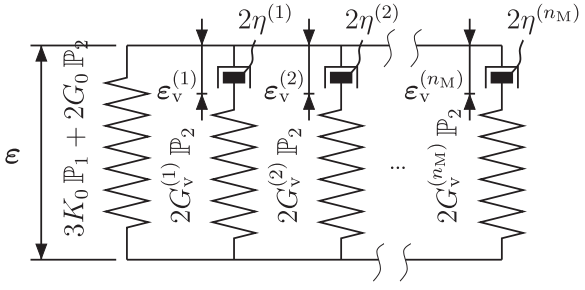

Fig. 2. Rheological model for the generalized Maxwell model.

$$\frac{\partial \psi}{\partial \boldsymbol{\varepsilon}_{\mathrm{v}}^{(m)}} + \frac{\partial \phi}{\partial \dot{\boldsymbol{\varepsilon}}_{\mathrm{v}}^{(m)}} = \mathbf{0} \tag{13}$$

or

$$\frac{G_{\mathrm{v}}^{(m)}}{\eta^{(m)}} \mathbb{P}_2[\boldsymbol{\varepsilon} - \boldsymbol{\varepsilon}_{\mathrm{v}}] = \dot{\boldsymbol{\varepsilon}}_{\mathrm{v}}^{(m)}. \tag{14}$$

The generalized Maxwell model gives rise to a characteristic creep curve when instantaneously loaded by a constant stress. In contrast, the instantaneous application of a constant shear strain results in stress relaxation. Figs. 3 and 4 illustrate the creep and relaxation response obtained using a single dashpot element ($n_{\mathrm{M}} = 1$).

In case of time-harmonic loading at angular frequency ω, the single-element Maxwell model gives rise to shear damping with torsional loss tangent

$$\tan(\delta_{\mathrm{G}}) = \frac{\mathrm{Im}(G^*(\omega))}{\mathrm{Re}(G^*(\omega))} = \frac{G_{\mathrm{v}}\,\eta\,\omega}{G_0\,G_{\mathrm{v}}^2 + (G_0 + G_{\mathrm{v}})\eta^2\,\omega^2}, \tag{15}$$

where $G^*(\omega)$ denotes the dynamic effective shear modulus. The torsional loss tangent exhibits a Debye peak with a maximum at frequency

$$f_{\mathrm{G,max}} = \frac{\omega_{\mathrm{G,max}}}{2\pi} = \frac{1}{2\pi}\frac{G_{\mathrm{v}}}{\eta}\sqrt{\frac{G_0}{G_0 + G_{\mathrm{v}}}}. \tag{16}$$

Analogously, the effective Young modulus of the linear viscoelastic model with one Maxwell element for a uniaxial tension test can be computed either directly by solving the time-harmonic boundary value problem or by exploiting isotropy and using the correspondence principle (Lakes, 1999). Both ways lead to the uniaxial loss tangent (with $\bar{G} = G_0 + G_{\mathrm{v}}$)

$$\tan(\delta_{\mathrm{E}}) = \frac{3G_{\mathrm{v}}^2 K_0 \eta\omega}{G_0 G_{\mathrm{v}}^2(G_0 + 3K_0) + \bar{G}(\bar{G} + 3K_0)\eta^2\omega^2}, \tag{17}$$

which peaks at a frequency of

$$\left.\begin{aligned} f_{\mathrm{E,max}} &= \frac{1}{2\pi}\frac{G_{\mathrm{v}}}{\eta}\sqrt{\frac{G_0}{\bar{G}}\frac{G_0 + 3K_0}{\bar{G} + 3K_0}} \\ &= f_{\mathrm{G,max}}\sqrt{\frac{G_0 + 3K_0}{\bar{G} + 3K_0}} \end{aligned}\right\}. \tag{18}$$

2.4. Microscale: particle–matrix composite

The material model summarized in Section 2.3 is used to model the individual phases on the microscale of the particle–matrix composite of interest. In particular, the aim is to identify qualitative and quantitative effects on the frequency-dependent damping induced by local material instabilities in the composite. In an attempt to mimic previous experiments, we consider an isotropic microstructure consisting of a lossy viscoelastic matrix material with linear viscoelastic inclusions showing a higher stiffness but smaller viscous effects. We assume the existence of a representative periodic unit cell containing 20 spherical inclusions (corresponding to 10% vol.), which is referred to as Volume Element (VE) in our study, see Fig. 6. It was verified that the VE has near-isotropic effective elastic moduli. Note that a much larger VE (in terms of the number of inclusions) could have been used. However, numerical investigations have shown that an increased VE size does not alter the results qualitatively, and that the quantitative influence is small. Although the chosen VE is thus not a representative VE in the strictest sense, the dissipative effects observed are the same irrespective of the number of inclusions. For the matrix phase we use the generalized Maxwell model with the material parameters of pure tin (Sn) summarized in Table 1. For simplicity we consider only a single Maxwell element ($n_{\mathrm{M}} = 1$) whose parameters are chosen to best fit experimental reality in the low-frequency regime which is of utmost importance in most structural applications. Fig. 5 shows experimental data of the loss tangent $\tan\delta$ of pure tin under time-harmonic torsional loading at ambient temperature over a wide range of frequencies (Cook and Lakes, 1995).

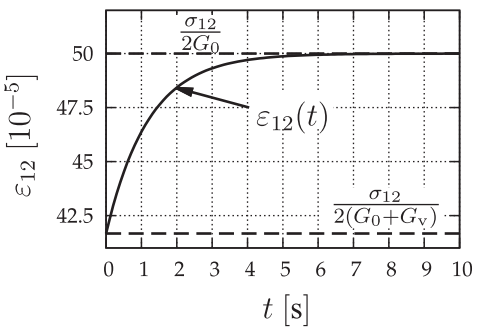

Fig. 3. Creep curve for instantaneously-applied constant shear stress σ_{12}.

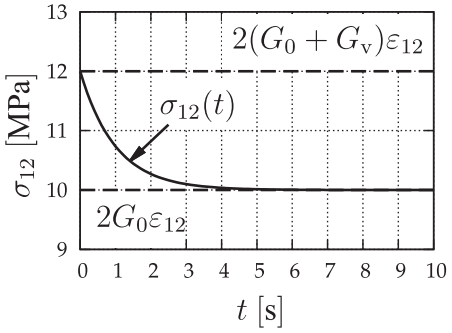

Fig. 4. Relaxation curve for instantaneously-applied constant shear strain ϵ_{12}.

The inclusion phase is assumed to undergo a structural transition that results in a local loss of stability. For example, according to theories of Landau (1937) and Devonshire (1949, 1951) ferroelectric perovskite ceramics such as barium titanate ($BaTiO_3$), the free energy landscape develops into a multi-well configuration upon cooling below the Curie temperature. When the high-temperature phase of the material is stabilized at lower temperatures below the Curie point, this results in non-positive-definite elastic moduli in the $BaTiO_3$ inclusions (Kochmann and Drugan, 2012; Wojnar and Kochmann, 2014). This was demonstrated experimentally by Jaglinski et al. (2007). A detailed model of the cubic-to-tetragonal transition in $BaTiO_3$ goes beyond the scope of the present paper (and the exact details of the phase transition are of minor importance). Instead, we assume the inclusions consist of a fictitious ceramic material derived from $BaTiO_3$. We adopt the shear modulus of approximately-isotropic polycrystalline $BaTiO_3$. Viscous effects in the ceramic inclusion phase at room temperature are somewhat smaller than in the tin matrix; e.g. the loss tangent in pure $BaTiO_3$ was measured near 0.01 in the low-frequency regime (Jaglinski and Lakes, 2007). Therefore, we treat the inclusion phase as linear viscoelastic and apply the same generalized Maxwell model with a different set of parameters which are summarized in Table 1.

Positive-definiteness of an isotropic solid requires that both shear and bulk moduli, G and K, respectively, are positive (Kirchhoff, 1859). The weaker condition of pointwise stability enforces strong ellipticity of the elastic modulus tensor, which for isotropic media is equivalent to requiring $G > 0$ and

Table 1
Viscoelastic material parameters for the matrix and inclusion materials.

Matrix (Sn)	G_0	18.43 GPa	K_0	58 GPa	$G_v^{(1)}$	1.843 GPa	$\eta^{(1)}$	1.843 GPa s
Inclusion ($\sim BaTiO_3$; $\alpha_c < \alpha \leqslant 1.845$)	G_{inc}	50 GPa	K_{inc}	αG_{inc}	$G_{inc,v}^{(1)}$	2.658 GPa	$\eta_{inc,v}^{(1)}$	0.412 GPa s

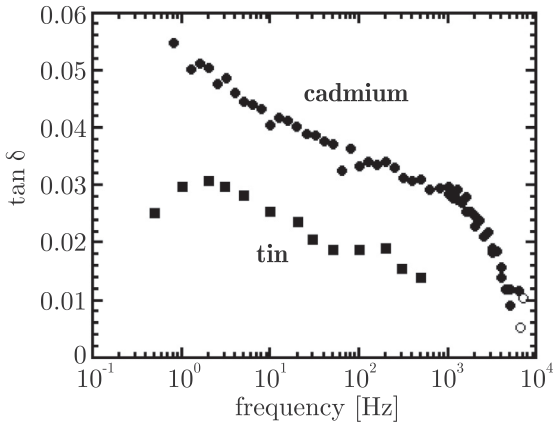

Fig. 5. Loss tangent tan δ vs. frequency for cadmium and tin at ambient temperature, modified after (Cook and Lakes, 1995).

$K > -4/3\,G$ (Lord Kelvin, 1856). Hence, the expected loss of positive-definiteness of the isotropic elastic moduli of the inclusion phase implies that its bulk modulus becomes negative while its shear modulus remains positive (see e.g. Kochmann and Drugan, 2012). To this end, the bulk modulus is varied from positive to negative values, until the composite loses stability. We introduce the tuning parameter α such that the elastic moduli in the inclusion phase are related by

$$K_{inc} = \alpha G_{inc}. \tag{19}$$

Stability of free-standing homogeneous solids (i.e. bodies with pure-traction or mixed boundary conditions) requires positive-definiteness of the elastic modulus tensor, which translates into $\alpha \geqslant 0$ for stability. In addition to this regime of unconditional stability, recent studies confirmed that non-positive-definite elastic phases can be stable if sufficiently constrained (Drugan, 2007; Kochmann and Drugan, 2009, 2012; Wojnar and Kochmann, 2014). Therefore, we here investigate the full range of $\alpha_{ref} \geqslant \alpha \geqslant \alpha_c$ with a critical value $\alpha_c < 0$ denoting the stability limit. Here, α_{ref} denotes the reference value of $BaTiO_3$ at room temperature, cf. Table 1. Experiments used polycrystalline, polydomain particles of $BaTiO_3$ to create an approximately isotropic volumetric eigen strain during transformation, which is here represented by the negative bulk modulus. In the following, we proceed to investigate the impact of the inclusions' bulk modulus on the overall damping properties of the material.

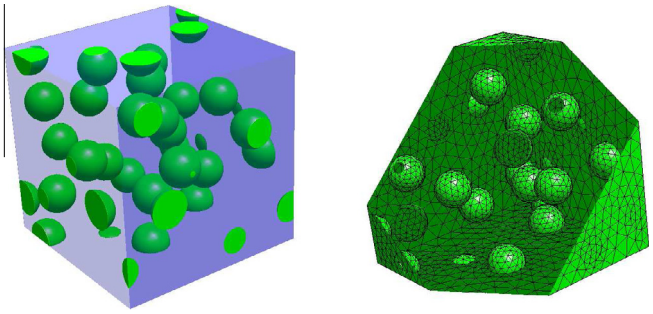

Fig. 6. Periodic VE containing 20 linear elastic, spherical inclusions (with a volume fraction of 10%) embedded into a viscoelastic matrix (left); finite element discretization using quadratic tetrahedra (right).

The VE on the microscale contains 20 spherical inclusions amounting to a total of approximately 10 vol.%. It is discretized using quadratic tetrahedral finite elements. Fig. 6 illustrates the geometry of the particle–matrix composite VE and its finite element discretization used for subsequent simulations.

Different mesh resolutions with up to 862,551 degrees of freedom have been compared in order to verify that the mesh density used in the simulations is sufficient (199,326 DOF; h_2). For $\alpha = -0.15$ and $f = 0.15$ Hz the normalized difference of $\bar{\epsilon}_{xx}(t)$ with respect to the finest discretization is shown in Fig. 7. Note that the error in the effective strain for mesh level h_1 is less than 0.1%, which justifies the chosen discretization level.

2.5. Two-scale problem and principles of homogenization

In the following, a classical two-scale formulation is used so that a clear separation of scales is hypothesized. This requires that field variables on the macroscale vary on a much bigger scale and much more slowly in space than those on the microscale. In other words, the structural or macroscopic scale is strictly separated from the microstructural scale where the material heterogeneities of the composite become apparent. Note that this essentially requires that the microstructural length scale is significantly smaller than the norm of the gradient of the mechanical fields on the macroscopic scale. Then, balance of momentum must be satisfied on the macroscopic scale with the macroscopic (or effective) stress tensor $\bar{\boldsymbol{\sigma}}$, the effective strain tensor $\bar{\boldsymbol{\varepsilon}}$, the effective mass density $\bar{\varrho}$ and the effective body force field $\bar{\boldsymbol{b}}$:

$$\left.\begin{array}{ll} \operatorname{div}_{\bar{\boldsymbol{x}}}[\bar{\boldsymbol{\sigma}}(\bar{\boldsymbol{x}},t)] + \bar{\boldsymbol{b}}(\bar{\boldsymbol{x}},t) & = \bar{\varrho}(\bar{\boldsymbol{x}},t)\,\ddot{\bar{\boldsymbol{u}}}(\bar{\boldsymbol{x}},t) \\ \bar{\boldsymbol{\sigma}}(\bar{\boldsymbol{x}},t) & = \bar{\boldsymbol{\sigma}}(\bar{\boldsymbol{x}},t)^{\mathrm{T}} \end{array}\right\}. \tag{20}$$

The structural problem is also equipped with suitable kinematic and static boundary conditions. As discussed above, the low frequencies studied in the sequel allow us to neglect inertial effects, and we neglect the effect of body forces.

The effective macroscopic stress and strain tensors $\bar{\boldsymbol{\sigma}}$ and $\bar{\boldsymbol{\varepsilon}}$ are fully determined by the microstructural characteristics and inelastic processes occurring in the VE. The coupling of scales is formally defined by volumetric averaging over the VE Ω with volume $|\,\Omega\,|$, i.e.

$$\bar{\boldsymbol{\sigma}} = \frac{1}{|\,\Omega\,|}\int_{\partial\Omega} \boldsymbol{t}\otimes\boldsymbol{x}\,\mathrm{d}A = \frac{1}{|\,\Omega\,|}\int_{\Omega}\boldsymbol{\sigma}\,\mathrm{d}V = \langle\boldsymbol{\sigma}\rangle, \tag{21}$$

$$\bar{\boldsymbol{\varepsilon}} = \frac{1}{|\,\Omega\,|}\int_{\partial\Omega} \operatorname{sym}(\boldsymbol{u}\otimes\boldsymbol{n})\,\mathrm{d}A = \frac{1}{|\,\Omega\,|}\int_{\Omega}\boldsymbol{\varepsilon}\,\mathrm{d}V = \langle\boldsymbol{\varepsilon}\rangle. \tag{22}$$

As a consequence, the effective constitutive model on the macroscopic scale derives from the microscopic material properties and the morphology and topology of the microstructure. Identifying the relation between the effective stress tensor and the history of the effective strain tensor yields the homogenized constitutive model of the micro-heterogeneous material. An overview of the microscopic and macroscopic equations describing the two-scale problem is given in Fig. 8. We follow classical procedures of numerical homogenization (see e.g. Kouznetsova et al., 2001; Miehe and

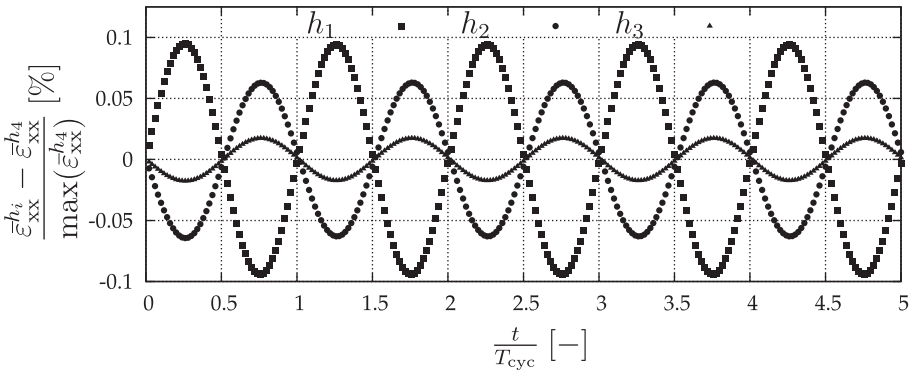

Fig. 7. Results of the mesh density study for $\alpha = -0.15$, $f = 0.15$ Hz.

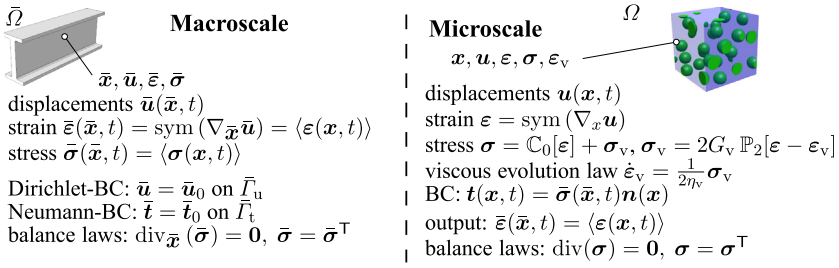

Fig. 8. Overview of the microscopic and macroscopic governing equations describing the two-scale boundary value problem.

Koch, 2002). The effective uniaxial response of the viscoelastic particle–matrix material is obtained by applying anti-periodic normal traction boundary conditions

$$\bar{\sigma}(t) = \sigma_0 \sin(2\pi f t)\, e_x \otimes e_x, \quad \sigma_0 = 50 \text{ MPa}, \tag{23}$$

in the e_x-direction at a prescribed driving frequency $f = \omega/2\pi$. This boundary condition mimics a cyclic uniaxial tension test. It allows for the extraction of the effective dynamic Young modulus and the corresponding loss tangent δ comparable to those measured experimentally in time-harmonic bending.

2.6. Stability considerations

To estimate the stability of the composites under investigation, let us consider elastic stability theory. The addition of viscous effects generally stabilizes and hardly destabilizes elastic systems (see e.g. Ziegler, 1953). Here, we will show that the elastic assumption is sufficient to provide a good estimate of the stability limit. As pointed before, pointwise stability of elastic solids requires the strong ellipticity of its elastic modulus tensor to ensure real-valued wave speeds of linear elastic stress waves. In addition, overall stability of a homogeneous elastic body requires the quasiconvexity of its strain energy density (or, for inhomogeneous solids in general, a unique minimizer to exist for a given set of boundary conditions). For homogeneous linear elastic solids under mixed displacement/traction boundary conditions this is equivalent to requiring positive-definiteness of the elastic modulus tensor. For an isotropic solid, this in turn enforces positive shear and bulk moduli. Therefore, as a free-standing, unconstrained solid, the inclusion phase would be unstable for $\alpha = K_{inc}/G_{inc} < 0$. However, when embedded in another stable matrix material, stability conditions must be verified for the overall composite. As shown e.g. by Kochmann and Drugan (2012), the stability of an elastic composite requires that the effective moduli of the composite satisfy positive definiteness (i.e., for isotropic composites, the effective shear and bulk moduli must be positive). As a consequence, the overall response of a microheterogeneous composite can be stable with a non-positive-definite inclusion phase (having a negative bulk modulus), as long as α is greater than some critical value α_c. This critical value is determined by enforcing that the effective bulk modulus be non-negative. For the chosen (approximately isotropic) microstructure, the lower Hashin–Shtrikman bound can be used to estimate the effective bulk modulus and thus to determine an estimate for α_c (for a discussion of the classical bounds in the presence of negative stiffness see Kochmann and Milton, in press). This yields the sought lower bound on the inclusion bulk modulus, viz.

$$\alpha = \frac{K_{inc}}{G_{inc}} > -\frac{4(1-c)K_0}{3K_0 + 4cG_0}\frac{G_0}{G_{inc}} = \tilde{\alpha}_c, \tag{24}$$

where c denotes the volume fraction of the inclusion phase. For the parameters provided in Table 1 and a volume fraction of $c = 10\%$, we obtain the estimate $\alpha_c \approx \tilde{\alpha}_c = -0.4243$. The lower bound for α thus depends on multiple microstructural characteristics: (i) the inclusion volume fraction, (ii) the elastic properties of the matrix material, (iii) the shear modulus of the inclusion phase, and (iv) the degree of isotropy of the effective composite material. Notably, the inclusion phase is predicted to be allowed a stable bulk modulus that is (significantly) less than zero. We note that we used the lower Hashin–Shtrikman bound to find a stability limit on the inclusion moduli by enforcing that the effective bulk modulus of the composite must be positive for stability. While the Hashin–Shtrikman bound is a valid lower bound on the effective moduli for this (approximately isotropic) composite, the above procedure is not guaranteed to lead to a lower bound on the inclusion bulk modulus' stability limit (the actual critical effective bulk modulus may deviate from the lower bound construction). This is especially true when considering the finite VE size. Yet, this lower bound is shown to be a remarkably good estimate.

Numerical experiments indicate that $\alpha_{min} = -0.425$ forms the stability limit for the specific microstructural representation chosen here (i.e., $\alpha_{min} = -0.425$ appears stable but no stable values $\alpha_{min} < -0.425$ could be identified). The fact that this

numerically-determined limit lies below the theoretical prediction above is no contradiction because the Hashin–Shtrikman bound assumes isotropy, which is approximately realized here (therefore the good match) but not entirely due to missing symmetry in the VE. As a side note, it has been long recognized and numerically verified that the lower Hashin–Shtrikman bound can provide accurate predictions for isotropic inclusion microstructures (see e.g. Fritzen and Böhlke (2011) for a numerical study of particle reinforced metal ceramic composites). For anisotropic materials more complex bounds have been derived (see e.g. Böhlke and Lobos, 2014).

2.7. Computational strategies

In order to speed up the finite element simulations, the repetitive nature of the mechanical fields occurring under cyclic loading is exploited. A preconditioned conjugate gradient method (HIPS, http://hips.gforge.inria.fr) is used to solve the linearized systems of equations (Gaidamour and Henon, 2008). A small dimensional set of reduced solution vectors is built during the simulation which is used to provide good initial values for the CG method by means of orthogonal projection involving the current stiffness matrix. Thereby, not only the number of iterations is reduced but it also allows to keep the same preconditioner for many subsequent load steps. The small dimension of 3 to 5 vectors for the reduced solution space clearly shows the self-similarity of the local mechanical fields. It indicates that the used finite element model is well-suited for sophisticated reduced basis methods such as the APHR (A Priori Hyper-Reduction; Ryckelynck, 2009), the viscoelastic NTFA (Fritzen and Böhlke, 2013) or the recent reduced basis model order-reduction scheme of Fritzen and Leuschner (2013) which can further improve the computational efficiency.

3. Effective dynamic material response

3.1. Computational setup

Simulations apply the antiperiodic traction boundary conditions (23) for uniaxial tension–compression to the microstructural VE shown in Fig. 6. Two parameters are varied over wide ranges: (i) the mechanical driving frequency f and (ii) the inclusion modulus ratio $\alpha \in [-0.425, \alpha_{\text{ref}}]$. Outputs of the simulations comprise the effective transient strain response in the axial and transverse directions, $\bar{\varepsilon}_{xx}(t)$, $\bar{\varepsilon}_{yy}(t)$ and $\bar{\varepsilon}_{zz}(t)$. The last load cycle (verified to be free of transient effects) is taken as a basis to generate the following effective material characteristics:

- the complex Young modulus $E_* = e^{i(\omega t+\delta)} \mid E_* \mid$,
- the complex Poisson ratio $\nu_* = e^{i(\omega t+\delta_\nu)} \mid \nu_* \mid_\pm$,
- the time-domain phase shift δ between $\bar{\sigma}_{xx}$ and $\bar{\varepsilon}_{xx}$.

The complex Young modulus can be decomposed into the storage modulus E' and the loss or dissipation modulus E'' defining the uniaxial loss tangent $\tan\delta$

$$E' = \mid E_* \mid \cos\delta, \qquad E'' = \mid E_* \mid \sin\delta, \quad \tan\delta = \frac{E''}{E'}. \tag{25}$$

In order to determine a suitable frequency range, the matrix material was analyzed individually and the frequency $f_{E,\max}$ at which the matrix material shows a peak of its uniaxial loss tangent $\tan\delta_E$ was identified as $f_{E,\max} \approx 0.15102$ Hz. Therefore, the frequency range of $f \in [0.0025\text{ Hz}, 1\text{ Hz}]$ was chosen for the subsequent computational studies along with inclusion modulus ratios of $\alpha \in [-0.425, 1.84506]$. In total, $15 \times 12 = 180$ transient FE simulations were carried out and the effective stress–strain curves were extracted for effective parameter identification.

Fig. 9 illustrates the transient response: shown are the uniaxial driving stress $\bar{\sigma}_{xx}(t)$ according to (23), the resulting uniaxial strain $\bar{\varepsilon}_{xx}(t)$ and the transverse strain component $\bar{\varepsilon}_{yy}(t)$ vs. normalized time for the example parameters $\alpha = -0.425$ and $f = 0.10$ Hz ($T_{\text{cyc}} = 1/f$ is the duration of one load cycle). It becomes apparent that the last load cycle has indeed stabilized and all transient effects have been removed effectively in the last cycle of the simulation, which allows for a clean extraction of the harmonic effective response.

The transient response decays quickly over the course of at most two load cycles, and the fourth and fifth cycles are identical up to numerical precision. Note that for Fig. 9 we deliberately chose a combination of parameters that gives rise to the most pronounced *swing-in* effect, i.e. other parameters are found to provide a stabilized response already in the second or third cycle. Based on these observations, we will apply five load cycles to the virgin, unloaded material in all simulations in order to attain stabilized cycles and to extract the effective response from the fifth cycle. As an example, the last cycle in Fig. 9 is plotted individually and compared to the harmonic response for the identified parameters, viz.

$$\bar{\varepsilon}_{xx}(t) = \frac{\sigma_0}{\mid E_* \mid} \sin(2\pi f t + \delta). \tag{26}$$

Fig. 9 shows an excellent agreement between both response functions, which confirms the high level of accuracy of the chosen numerical approach and the choice of the fifth load cycle as representative for time-harmonic loading.

3.2. Effective dynamic material properties

The absolute value of the effective complex Young modulus $\mid E_* \mid$ and the signed dynamic Poisson ratio $\mid \nu_* \mid_\pm$ of the particle–matrix composite are shown in Fig. 10 for all actuation frequencies and for the full parameter range of α investigated in this study. For values of $\alpha \geqslant 0$, dynamic effects appear significantly less pronounced and only marginal variations in the two effective material parameters E_*, ν_* are observed due to the small volume fraction of the inclusion phase. For $\alpha = \alpha_{\text{ref}}$ (i.e. for literature values of stable $BaTiO_3$ at ambient temperature) the peak value of 58.99 GPa for the dynamic Young modulus is attained approximately at $f = 1$ Hz in the range of interest. For $\alpha < 0$ a qualitative change of results is observed. As can be expected (see e.g. Kochmann, 2014), the composite softens dramatically as the inclusion phase approaches the stability limit. The smallest value of the effective Young modulus, 14.07 GPa, is found at $f = 0.0025$ Hz for $\alpha = -0.425$, and it is approximately four times smaller than the reference value at $\alpha = \alpha_{\text{ref}}$. Furthermore, for $\alpha < 0$ effective moduli vary considerably more with frequency. This becomes obvious from Table 2, which includes the ratio of minimum to maximum dynamic Young modulus for each value of α.

These results confirm what was observed previously in simple one-dimensional examples as well as based on composite property bounds (Lakes, 2001a,b; Wang and Lakes, 2004a,b; Wang et al., 2006; Kochmann, 2014): even at low volume fractions, a non-positive-definite phase can dramatically alter the effective viscoelastic composite properties. In particular, the negative compressibility of the inclusions considerably amplifies the dynamic damping. Such behavior is not observed for the different (non-negative) values of α, i.e. for $0 \leqslant \alpha \leqslant \alpha_{\text{ref}}$, where the variation of effective moduli and damping is much smaller. This cannot be explained merely by the change in inclusion bulk modulus. Instead, it hints at a change of dynamic microstructural mechanisms.

The material's damping capacity under harmonic loading is primarily described by the time-domain phase shift δ (or the loss tangent $\tan\delta$) and the loss modulus $E'' = \mid E_* \mid \sin\delta$. The loss modulus

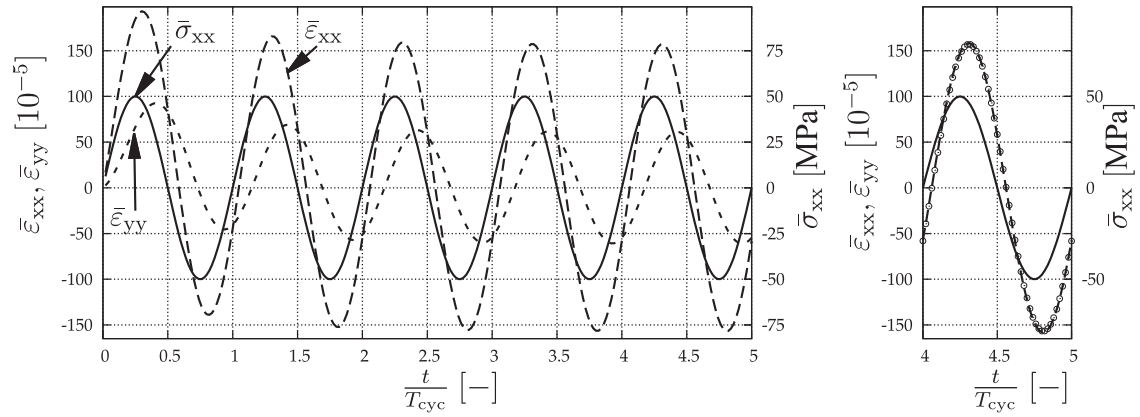

Fig. 9. Transient effective stress–strain response versus time for $\alpha = -0.425$ and $f = 0.1$ Hz; left: entire stress–strain history; right: last cycle only. Shown are $\bar{\varepsilon}_{xx}$ (dots and dashed line) and $\bar{\sigma}_{xx}$ (solid line); the dots represent numerical values, the dashed line represents the theoretical response based on the identified effective material parameters E_* and δ.

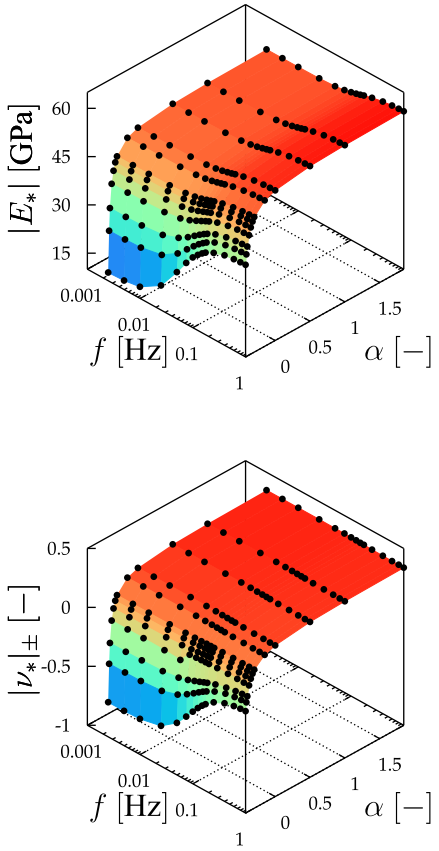

Fig. 10. Absolute value of the complex Young modulus and signed dynamic Poisson ratio $|\nu_*|_\pm$ for all 180 simulations.

is shown in Fig. 11 as a function of modulus ratio α and frequency f (the left graphic shows $\alpha < -0.30$, the middle $\alpha \geqslant -0.30$, and the right graphic shows the full range of this investigation). For comparison, the loss tangent is shown in Fig. 11, and it exhibits the same qualitative behavior as the loss modulus. While the storage modulus E' and the dynamic modulus $|E_*|$ decrease towards the stability limit near $\alpha = -0.425$, the loss modulus peaks at this value with a maximum of 12.45 GPa at a frequency of 0.075 Hz. The maximum phase shift with $\tan\delta = 0.555$ occurs at 0.05 Hz. Both values are remarkable when considering the reference values of the pure matrix and inclusion materials: according to relations (17) and (18), the maximum loss modulus of tin is 2.23 GPa and

Table 2
Minimum and maximum dynamic modulus $|E_*|$ and the ratio thereof as functions of α.

α	$\min_f \|E_*\|$ (GPa)	$\max_f \|E_*\|$ (GPa)	min/max
−0.4250	12.65	38.65	3.0549
−0.4125	25.44	41.72	1.6400
−0.4000	32.33	44.03	1.3617
−0.3750	39.58	47.23	1.1935
−0.3500	43.34	49.36	1.1389
−0.3250	45.64	50.87	1.1144
−0.3050	47.20	51.99	1.1015
−0.1500	51.17	55.35	1.0817
0.0000	52.51	56.67	1.0792
0.5000	53.95	58.21	1.0791
1.0000	54.39	58.73	1.0797
α_{ref}	54.71	59.10	1.0803

the peak loss tangent $\tan\delta = 0.0429$, which occur at a frequency of $f_{E,\max} = 0.151027$ Hz (the ceramic inclusion phase shows maximum damping in bending of approximately $\tan\delta = 0.0218$) in the present material model. For $\alpha \geqslant 0$ the peak loss modulus and phase shift agree well with those of the pure matrix material. As soon as $\alpha < 0$, the frequency at which the peak loss modulus and the peak loss tangent are observed shifts considerably towards lower frequencies. At the stability limit of $\alpha = -0.425$ the peak frequency has reduced by more than half compared to that of the pure matrix or of the composite with $\alpha \geqslant 0$. The shift in frequency is in contradiction to common observations reported, e.g. by Staub et al. (2012) who consequently made the assumption that the relaxation time of the heterogeneous material matches the one of the viscoelastic constituent. Our study shows that the transient response for $\alpha < 0$ violates this assumption.

Our numerical results for the effective dynamic storage and loss moduli agree surprisingly well with the following estimates for an isotropic two-phase composite. Consider an assemblage of coated spherical particles for which Hashin and Shtrikman (1963) derived closed-form bounds on the effective elastic moduli of the resulting isotropic composite. We consider an isotropic two-phase composite consisting of linear viscoelastic inclusions embedded in a linear viscoelastic matrix with properties given by Table 1. For each phase, we can translate the listed Maxwell model parameters into the complex-valued frequency-dependent bulk and shear moduli for time-harmonic loading with frequency f, viz., respectively,

$$K^* = K_0, \quad G^* = G_0 + \frac{i2\pi f G_1 \eta}{G_1 + i2\pi f \eta}. \tag{27}$$

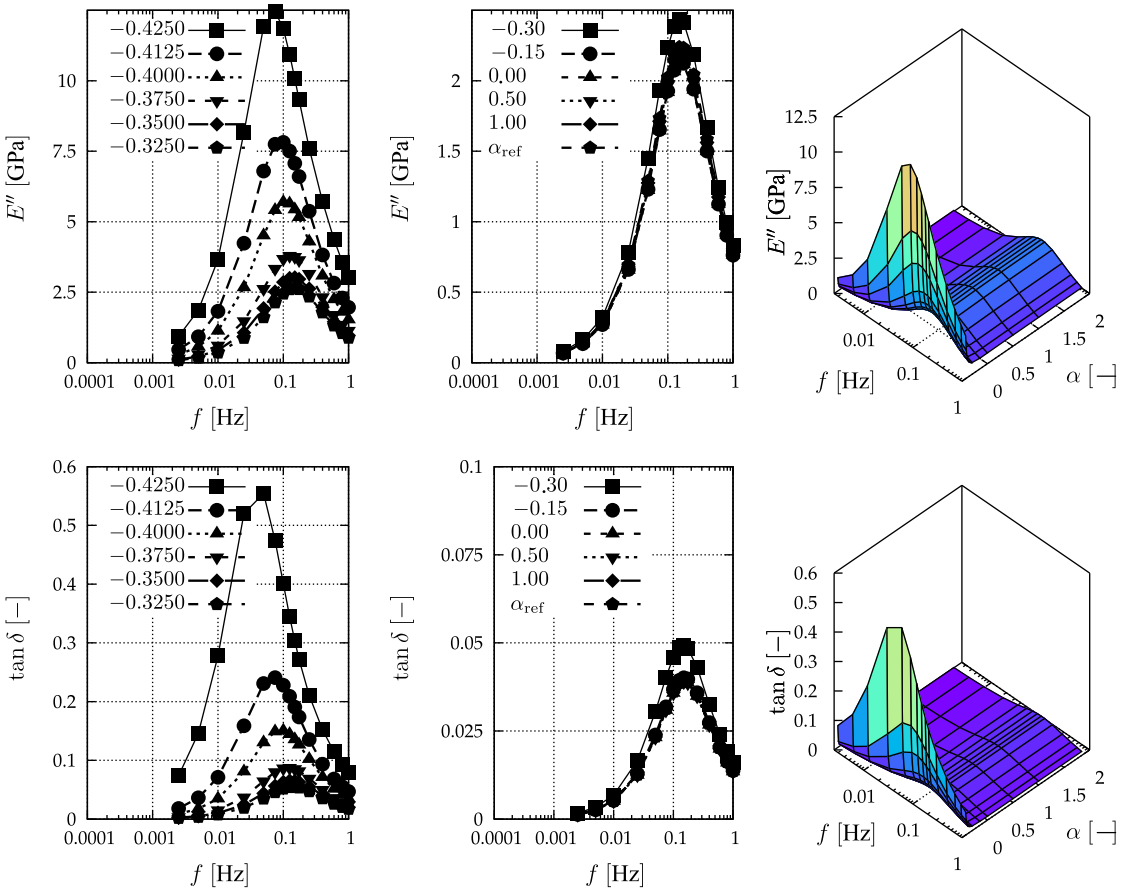

Fig. 11. Uniaxial loss modulus E'' (top) for $\alpha < -0.30$ (left) and $\alpha \geqslant -0.30$ (middle), and three-dimensional representation (right) and loss tangent $\tan\delta$ (bottom) for $\alpha - 0.30$ (left) and $\alpha \geqslant -0.30$ (middle), and three-dimensional representation (right).

Since we neglect inertial effects, we can use the correspondence principle (Read, 1950; Lee, 1955) and hence apply the classical bounds of Hashin and Shtrikman (1963). By feeding the complex-valued moduli for both phases into the Hashin–Shtrikman lower bound, we compute the effective complex-valued dynamic Young modulus of the composite whose absolute value (the dynamic modulus) and whose imaginary part (the loss modulus) are shown in Fig. 12. The good qualitative agreement with the numerical data of Figs. 10 and 11 becomes apparent. A quantitative agreement is not fully achieved but is also not expected since the lower Hashin–Shtrikman bound only provides an estimate for the effective composite properties.

3.3. Transient stress strain curve

In order to better understand the high loss modulus and phase shift observed close to $\alpha = \alpha_c$ at frequencies near 0.10 Hz, let us investigate the time-dependent strain components in the x- and y-directions in more detail. Fig. 13 compares the strain responses for $\alpha = -0.425$ and for $\alpha = 0$. The phase shift between the

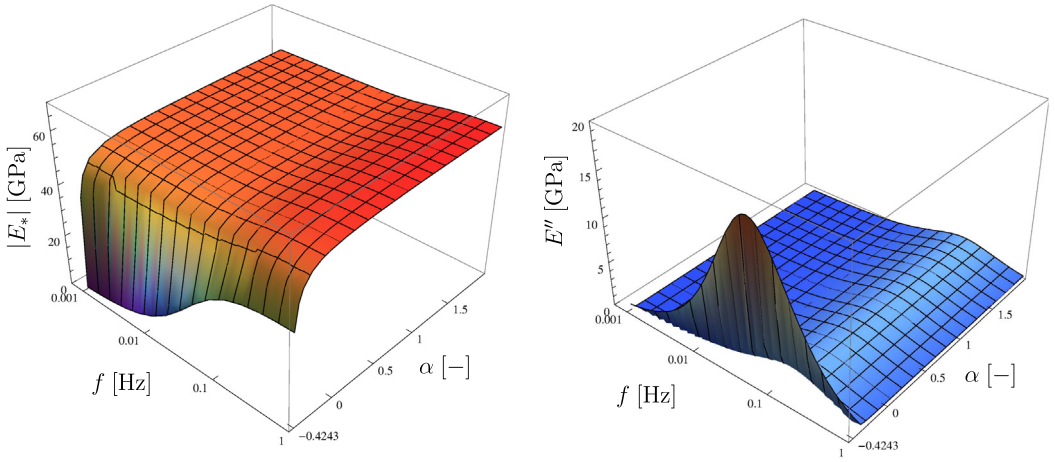

Fig. 12. Absolute value of the effective complex Young modulus $|E^*|$ and effective uniaxial loss modulus E'' of an isotropic Hashin–Shtrikman composite with the material parameters of Table 1 (using the correspondence principle to arrive at complex-valued viscoelastic moduli).

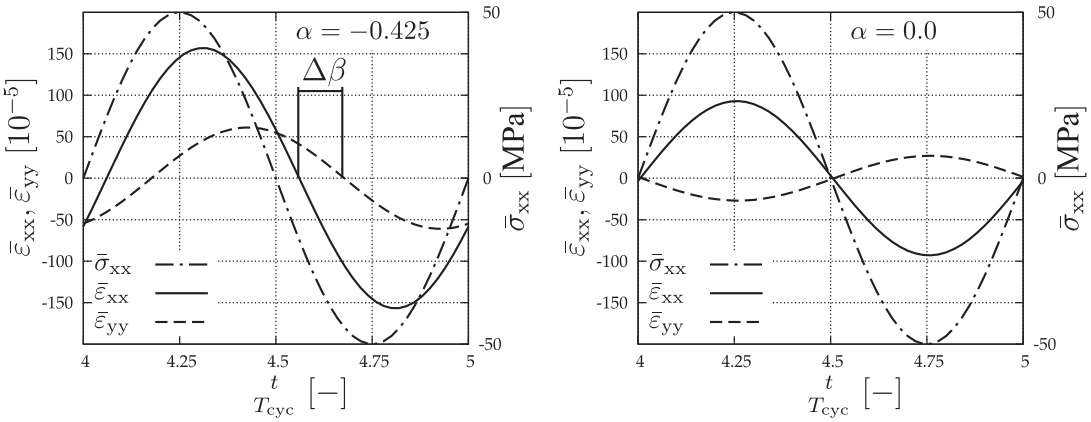

Fig. 13. Comparison of the time-dependent strain response for $\alpha = -0.425$ (left) and $\alpha = 0.0$ (right) at a frequency of 0.1 Hz. In the left graph, observe the phase shift $\Delta\beta$ between $\bar{\varepsilon}_{xx}$ and $\bar{\varepsilon}_{yy}$, and the same of sign of $\bar{\varepsilon}_{xx}$ and $\bar{\varepsilon}_{yy}$ (indicating auxeticity).

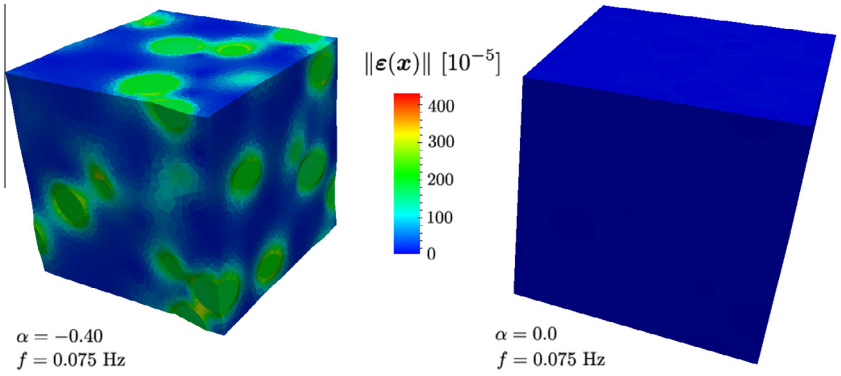

Fig. 14. The deformed VE at the end of the fifth load cycle (deformation is scaled by a factor of 200). Left: for $\alpha = -0.40$ a heterogeneous strain distribution is observed with peak values near the inclusions; right: for $\alpha = 0$ hardly any deformation remains (both graphics use the same color code).

longitudinal strain $\bar{\varepsilon}_{xx}$ and the transverse strain $\bar{\varepsilon}_{yy}$ is denoted by $\Delta\beta$. For $\alpha = -0.425$ it amounts to 0.730 (or 41.9°) whereas it is vanishingly small for the simulation with $\alpha = 0$. Another noteworthy difference is found in the sign of the transverse strains. While for non-negative or moderately negative α an overall lateral contraction is observed under uniaxial tension, lateral expansion is found when α approaches α_c. Notice also that for $\alpha \to \alpha_c$, the signs of $\bar{\varepsilon}_{xx}$ and $\bar{\varepsilon}_{yy}$ are observed to be identical in Fig. 13. This implies a negative value of the effective dynamic Poisson ratio, also known as *auxetic* behavior (see e.g. Evans et al., 1991; Lakes, 1987). The dynamic auxetic effect for low values of α also becomes apparent from Fig. 10. Auxeticity can be expected since, in a homogeneous isotropic linear elastic solid, Poisson's ratio $\nu \to -1$ as the bulk modulus $K \to 0$. Here, we consider a two-phase composite whose stability limit corresponds to a vanishing effective bulk modulus of the composite, so that we may expect a negative (static) effective Poisson's ratio before the composite loses stability.

3.4. Local stress and strain fields

The dramatic change in the effective response hints at a change of underlying physical mechanisms on the microscale. Therefore, let us investigate the inhomogeneous stress and strain distribution within the VE in more detail. To highlight the viscous mechanisms, the deformed state at the end of the last load cycle is investigated, i.e. at a time when the effective stress applied to the VE is zero while the deformation is non-zero due to the viscous strains that developed during the preceding load cycles. Fig. 14 compares the strain distribution (i.e., the norm of the strain tensor) for $\alpha = 0$ and $\alpha = -0.4$. At the investigated frequency of 0.075 Hz the phase shift for non-negative α is vanishingly small. Hence, the viscous strains are in phase with the applied stress and thus zero at the end of the load cycle. For $\alpha < 0$, the strain field appears to be significantly more heterogeneous, displaying large viscous deformation of the matrix in the vicinity of the inclusions. Here, the local strains near the interface between matrix and inclusions outmax the peak macroscopic longitudinal strain during the load cycle by a factor of ≈3. The high degree of heterogeneity of the deformation is considered as the main reason for the extraordinary damping of the composite. In other words, for $\alpha < 0$ (and close to the stability limit) the macroscopic uniaxial deformation is translated into considerably larger and heterogeneous microscopic deformation which creates high strains and consequently stresses concentrated around the inclusions. These in turn give rise to large viscous strains in the viscoelastic matrix near the interface, which ultimately leads to dramatically-increased damping on the macroscale.

By performing the same simulations in the absence of viscous effects in the inclusion phase, we have observed that the viscosity of $BaTiO_3$ indeed has a negligible impact on the strong increases in overall damping of the composite near the stability limit. Of course, the base damping of the composite changes according to classical composite mixture rules. However, the extreme damping increases shown above due to the non-positive-definite inclusion phase close to the stability limit remain almost unaffected upon removing the inclusion phase viscosity. In fact, this confirms that the observed strong damping increases in our model result solely from the large viscous strains in the matrix.

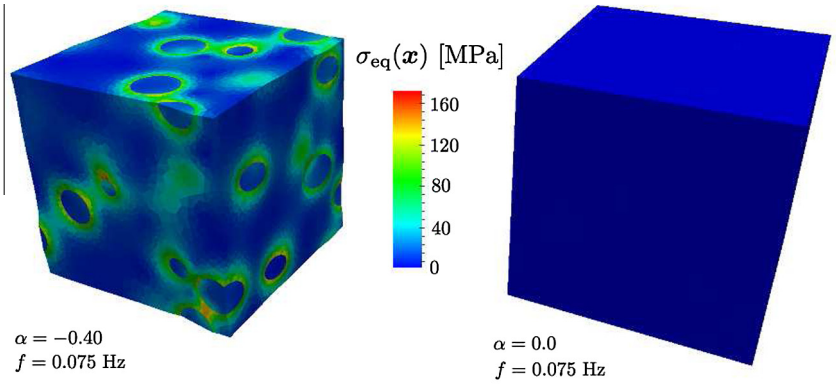

Fig. 15. Von Mises equivalent stress in the VE at the end of the fifth load cycle (deformation is scaled by a factor of 200). Left: for $\alpha = -0.40$ the surroundings of the inclusions show large stresses and are likely to exhibit inelastic deformation; right: for $\alpha = 0$ no notable stresses remain.

The high local strain fields and the associated high local stress fields shown in Fig. 15 can potentially lead to inelastic processes occurring near the material interfaces. Experiments have indicated that the high-stiffness and high-damping phenomena, e.g. in Sn–$BaTiO_3$ composites (Kochmann, 2006; Jaglinski et al., 2007), degrade with an increasing number of thermal cycling (where each thermal cycle produces one instance of negative-stiffness in the inclusion phase due to a delayed phase transition). This behavior was theorized to stem from localized damage and plastic deformation in the matrix near the inclusion interfaces. Our computational study here shows that (even at zero mean stresses in the VE) the local von Mises equivalent stress can reach more than twice the maximum applied stress during the load cycle. Hence, it is likely that the interface between metallic matrix and ceramic inclusions will degrade and debonding occurs with increasing number of load cycles. When particle–matrix decohesion is prevented, one is likely to observe micro-plasticity close to the matrix-inclusion interface. Under cycling loading, such micro-plasticity can e.g. induce cellular sub-grain structures in the metal phase due to dislocation nucleation and rearrangement, which leads to a local change of the mechanical properties of the matrix. In particular, a local embrittlement due to an increasing defect density may eventually result in matrix failure close to the particles. Again, the load magnitude is not critical but its repeated occurrence over many load cycles.

4. Summary and conclusions

Through a computational study, we have shown that the effective viscoelastic performance of metal–matrix composites with ceramic inclusions can vary significantly if the inclusion phase develops stable non-positive-definite elastic moduli. This phenomenon has been observed experimentally when a phase-transforming inclusion phase is embedded in a stiff matrix which temporarily prevents the transformation, resulting in stabilized inclusions with negative incremental elastic moduli. Going beyond all previous theoretical–numerical investigations, we here conducted a three-dimensional two-scale study based on linear viscoelastic models in both composite phases and we summarized the effect of a temporarily negative inclusion bulk modulus on the overall composite performance. Among others, we showed that close to the stability limit (i.e. before the inclusion becomes unstable) the overall composite damping increases significantly beyond what can be expected from either composite constituent. The non-positive-definite inclusion phase not only results in extreme increases of the effective loss modulus but also shifts the peak damping frequency to considerably lower frequencies. This behavior can be traced back to a change in microstructural damping mechanisms: while in conventional composites damping results from the individual contributions of all constituents following a rule of mixture (so that classical composite estimates apply), we here observe large localized viscous strains near the inclusion interfaces. Instead of reducing the overall damping of the composite, the inclusion phase promotes damping by displaying significant volumetric deformation which leads to increased damping by the matrix phase surrounding the inclusions. Among others, we have also reported negative dynamic Poisson's ratio (dynamic auxeticity) as a result of non-positive-definite inclusions near the loss of stability. Our computational findings support the applicability of the Hashin–Shtrikman bound as an appropriate estimate for the effective properties when combined with the correspondence principle. Due to the good match of analytical findings and numerical results, the computationally-inexpensive analytical estimates can be used to predict the damping properties of the studied class of materials with moderate variations of parameters such as the inclusion volume fraction or the respective elastic moduli. Finally, it is important to note that the observed phenomena occur while the inclusion phase softens dramatically when approaching the stability limit. Once the inclusion phase undergoes its full transformation, other dissipative mechanisms associated with the structural transition play a major role which have not been accounted for here.

Acknowledgements

F. Fritzen acknowledges financial support in the context of the YIG Computer Aided Material Modeling from the Karlsruher Institute of Technology (KIT) through the Excellence Initiative of the German Research Foundation (DFG). D.M. Kochmann acknowledges support from the National Science Foundation (NSF) through CAREER award CMMI-1254424.

References

Böhlke, T., Lobos, M., 2014. Representation of Hashin–Shtrikman bounds of cubic crystal aggregates in terms of texture coefficients with application in materials design. Acta Mater. 67, 324–334.
Cook, L.S., Lakes, R.S., 1995. Damping at high homologous temperature in pure Cd, In, Pb, and Sn. Scr. Metall. Mater. 32, 773–777.
Devonshire, A., 1949. XCVI. theory of barium titanate. Philos. Mag. Ser. 7 40 (309), 1040–1063.
Devonshire, A., 1951. CIX. theory of barium titanate: Part II. Philos. Mag. Ser. 7 42 (333), 1065–1079.
Dong, L., Stone, D., Lakes, R.S., 2010a. Softening of bulk modulus and negative poisson ratio in barium titanate ceramic near curie point. Philos. Mag. Lett. 90, 23–33.
Dong, L., Stone, D.S., Lakes, R.S., 2010b. Anelastic anomalies and negative poisson's ratio in tetragonal $BaTiO_3$ ceramics. Appl. Phys. Lett. 96 (14).

Drugan, W.J., 2007. Elastic composite materials having a negative stiffness phase can be stable. Phys. Rev. Lett. 98, 055502.
Evans, K.E., Nkansah, M.A., Hutchinson, I., Rodgers, S.C., 1991. Molecular network design. Nature 353, 124–125.
Fritzen, F., Böhlke, T., 2011. Periodic three-dimensional mesh generation for particle reinforced composites with application to metal matrix composites. Int. J. Solids Struct. 48, 706–718.
Fritzen, F., Böhlke, T., 2013. Reduced basis homogenization of viscoelastic composites. Compos. Sci. Technol. 76, 84–91.
Fritzen, F., Leuschner, M., 2013. Reduced basis hybrid computational homogenization based on a mixed incremental formulation. Comput. Methods Appl. Mech. Eng. 260, 143–154.
Gaidamour, J., Henon, P., 2008. A parallel direct/iterative solver based on a Schur complement approach. In: 11th IEEE International Conference on Computational Science and Engineering, 2008. CSE '08, pp. 98–105.
Germain, P., 1973. The method of virtual power in continuum mechanics. Part 2: Microstructure. SIAM J. Appl. Math. 25 (3), 556–575.
Hadamard, J., 1903. Lecons sur la propagation des ondes et les équations de l'hydrodynamique. Hermann, Paris.
Halphen, B., Nguyen, Q., 1975. Sur les matériaux standards generalisés. J. Méc. 14, 39–63.
Hashin, Z., Shtrikman, S., 1963. A variational approach to the theory of the elastic behaviour of multiphase materials. J. Mech. Phys. Solids 11, 127–140.
Holzapfel, G.A., Simo, J.C., 1996. A new viscoelastic constitutive model for continuous media at finite thermomechanical changes. Int. J. Solids Struct. 33 (20–22), 3019–3034.
Jaglinski, T., Lakes, R., 2007. Negative Stiffness and Negative Poisson's Ratio in Materials which Undergo a Phase Transformation. John Wiley & Sons Ltd., pp. 231–246.
Jaglinski, T., Kochmann, D., Stone, D., Lakes, R.S., 2007. Composite materials with viscoelastic stiffness greater than diamond. Science 315 (5812), 620–622.
Kirchhoff, G., 1859. Über das Gleichgewicht und die Bewegung eines unendlich dünnen elastischen Stabes. J. Reine Angew. Math. 56, 285–313.
Kochmann, D.M., 2006. Composite Materials with Inclusions of Negative-Stiffness: Theoretical Analysis and Experimental Investigations (Ph.D. thesis). University of Wisconsin–Madison, Master's thesis.
Kochmann, D.M., 2012. Stability criteria for continuous and discrete elastic composites and the influence of geometry on the stability of a negative-stiffness phase. Phys. Status Solidi B 249, 1399–1411.
Kochmann, D.M., 2014. Stable extreme damping in viscoelastic two-phase composites with non-positive-definite phases close to the loss of stability. Mech. Res. Commun. 58, 36–45.
Kochmann, D.M., Drugan, W.J., 2009. Dynamic stability analysis of an elastic composite material having a negative-stiffness phase. J. Mech. Phys. Solids 57 (7), 1122–1138.
Kochmann, D.M., Drugan, W.J., 2012. Analytical stability conditions for elastic composite materials with a non-positive-definite phase. Proc. R. Soc. A 468, 2230–2254.
Kochmann, D.M., Milton, G.W., in press. Rigorous bounds on the effective moduli of composites and inhomogeneous bodies with negative-stiffness phases. J. Mech. Phys. Solids, http://dx.doi.org/10.1016/j.jmps.2014.06.010.
Kouznetsova, V., Brekelmans, W.A.M., Baaijens, F.P.T., 2001. An approach to micro–macro modeling of heterogeneous materials. Comput. Mech. 27, 37–48.
Lakes, R.S., 1987. Foam structures with a negative Poisson's ratio. Science 235, 1038–1040.
Lakes, R.S., 1999. Viscoelastic Solids. CRC Mechanical Engineering Series. CRC Press.
Lakes, R.S., 2001a. Extreme damping in compliant composites with a negative-stiffness phase. Philos. Mag. Lett. 81 (2), 95–100.
Lakes, R.S., 2001b. Extreme damping in composite materials with a negative stiffness phase. Phys. Rev. Lett. 86, 2897–2900.
Lakes, R.S., Drugan, W.J., 2002. Dramatically stiffer elastic composite materials due to a negative stiffness phase? J. Mech. Phys. Solids 50 (5), 979–1009.
Lakes, R.S., Lee, T., Bersie, A., Wang, Y., 2001. Extreme damping in composite materials with negative-stiffness inclusions. Nature 410 (6828), 565–567.
Landau, L., 1937. On the theory of phase transitions (in russian). Zh. Eksp. Teor. Fiz. 7, 19–32.
Lee, E., 1955. Stress analysis in visco-elastic bodies. Q. Appl. Math. 13, 183.
Lord Kelvin (Thomson, W.), 1856. Elements of a mathematical theory of elasticity. Philos. Trans. R. Soc. London 146, 481–498.
Miehe, C., Koch, A., 2002. Computational micro-to-macro transitions of discretized microstructures undergoing small strains. Arch. Appl. Mech. 72, 300–317.
Milton, G.W., 2002. Theory of Composites. Cambridge University Press, Cambridge, England.
Ortiz, L., Stainier, L., 1999. The variational formulation of viscoplastic constitutive updates. Comput. Methods Appl. Mech. Eng. 171, 419–444.
Perić, D., 1993. On a class of constitutive equations in viscoplasticity: formulation and computational issues. Int. J. Numer. Methods Eng. 36 (8), 1365–1393.
Read, W., 1950. Stress analysis for compressible viscoelastic materials. J. Appl. Phys. 21, 671–674.
Reuss, A., 1929. Berechnung der Fließgrenze von Mischkristallen auf Grund der Plastizitätsbedingung für Einkristalle. Z. Angew. Math. Mech. 9, 49–58.
Ryckelynck, D., 2009. Hyper-reduction of mechanical models involving internal variables. Int. J. Numer. Methods Eng. 77 (1), 75–89.
Staub, S., Andrä, H., Kabel, M., Zangmeister, T., 2012. Multi-scale simulation of viscoelastic fiber-reinforced composites. Tech. Mech. 32 (1), 70–83.
Voigt, W., 1889. Über die Beziehung zwischen den beiden Elastizitätskonstanten isotroper Körper. Wied. Ann. 38, 573–587.
Wang, Y., Lakes, R.S., 2004a. Extreme stiffness systems due to negative stiffness elements. Am. J. Phys. 72 (1), 40–50.
Wang, Y.-C., Lakes, R.S., 2004b. Stable extremely-high-damping discrete viscoelastic systems due to negative stiffness elements. Appl. Phys. Lett. 84 (22), 4451–4453.
Wang, Y.-C., Swadener, J.G., Lakes, R.S., 2006. Two-dimensional viscoelastic discrete triangular system with negative-stiffness components. Philos. Mag. Lett. 86 (2), 99–112.
Wiechert, E., 1893. Gesetze der elastischen Nachwirkung für constante Temperatur. Ann. Phys. 286 (335–348), 546–570.
Wojnar, C.S., Kochmann, D.M., 2014. Instability of extreme static and stability of extreme dynamic effective stiffness of composites having a negative-stiffness phase. Philos. Mag. 94, 532–555.
Ziegler, H., 1953. Linear elastic stability. Z. Angew. Math. Phys. 4, 167–185.